Electronic Supplementary Material (ESI) for Energy & Environmental Science.

Supporting Information:

Predicting and Optimising the Energy Yield of Silicon-Perovskite Tandem Solar Cells under Real World Conditions

Maximilian T. Hörantner and Henry J. Snaith*

University of Oxford, Clarendon Laboratory, Parks Road, Oxford, OX1 3PU, United Kingdom

*henry.snaith@physics.ox.ac.uk

Methods

The simulation process consists of various steps which are illustrated in Figure S1 for the calculation of the power conversion efficiency and Figures S4, S5 for the simulation of the expected annual energy yield in real world conditions. The core of the optical model is based on the generalized transfer matrix method[1,2]. The constant refractive index of every material of the layers must be known, and together with the thicknesses of the layers and the incident radiation angle as parameters, the model output is the electric field distribution within the entire stack. This is used to calculate the fraction of transmitted and reflected light as well as the absorption within each layer. The model was implemented with the python programming language with heavy usage of the numerical computation package numpy. By calculating the absorption for every wavelength within the solar spectral range and assuming an internal quantum efficiency of 100%, which is feasible to do for perovskites solar cells according to published results[3,4], we end up with the external quantum efficiency for the absorbing layers.

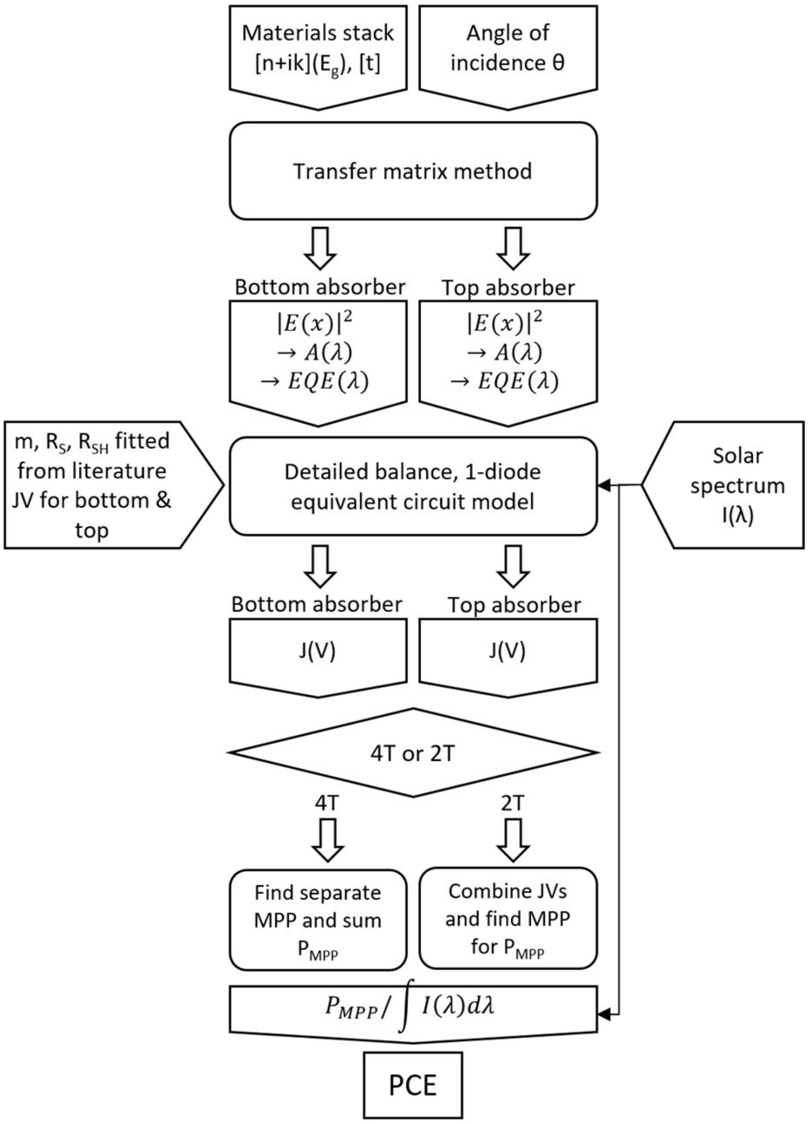

Figure S1: Simulation process for PCE calculation of tandem solar cell stack.

The material specific refractive index data for the applied materials was adopted from tandem modelling literature[5]. Changes of the bandgap for the perovskite layer have been simulated by assuming a perfect horizontal shift of the published absorption coefficient[6] along the energy axis. McMeekin et al.[7] have demonstrated that the absorption spectrum behaves in such a way in reality when different perovskite material compositions are used. The shifted absorption coefficient $\alpha(\lambda)$ can then be rearranged to calculate the extinction coefficient $k(\lambda)$ via,

$$k = \frac{\alpha\lambda}{4\pi}$$

which can be transformed to the refractive index n(λ) via the Kramers-Kronig transformation[8,9]:

$$n(E) - 1 = \frac{2}{\pi}\int_0^{\infty} \frac{E'k(E')}{E'^2 - E^2} dE'$$

The EQE's of both absorbing layers can further be used to determine the modelled J(V) characteristic with detailed balance theory[10]. Following the single diode equivalent circuit model and the reciprocity relation between photovoltaic quantum efficiency and electroluminescent emission efficiency (EQE_{EL})[11], we can derive the accurate J(V) characteristic representation. The inclusion of radiative efficiency allows us to account for recombination losses, and therefore for the realistic determination of V_{OC}. The combined J(V) equation becomes:

$$J(V) = J_{SC} - \frac{J_0(T)}{EQE_{EL}}\left(e^{\frac{q(V + J(V)R_S))}{mkT}} - 1\right) - \frac{V + J(V)R_S}{R_{SH}} \qquad (1)$$

where q, k, m, T, R_S, R_{SH} and EQE_{EL} are respectively the electron charge, Boltzmann's constant, ideality factor, cell temperature, series resistance, shunt resistance and average electroluminescent emission quantum efficiency. The short-circuit density (J_{SC}) and the reverse saturation current (J_0) can be determined by using the equations:

$$J_{SC} = q\int_0^{\infty} EQE(E)\phi_{sun}(E)dE \qquad (2)$$

and

$$J_0(T) = q\int_0^\infty EQE(E)\phi_{BB}(E,T)dE \quad (3)$$

where ϕ_{sun} and ϕ_{BB} are respectively the photon flux from the solar spectrum and the photon flux from a black body at temperature *T* and energy *E*, which is defined by Planck's law as:

$$\phi_{BB}(E,T) = \frac{1}{4\pi^2\hbar^3c^2}\frac{E^2}{exp\left(\frac{E}{kT}\right) - 1} \quad (4)$$

where *c* and $\hbar$ are speed of light and Planck's constant divided by 2π, respectively. We see that the second term on the right side of equation (1), which is also known as the dark current, is heavily influenced by J_0 and EQE_{EL}. J_0 is defined by the integral of the overlapping black body radiation with the EQE response of a solar cell, which we demonstrate in Figure S2 for T = 300 K.

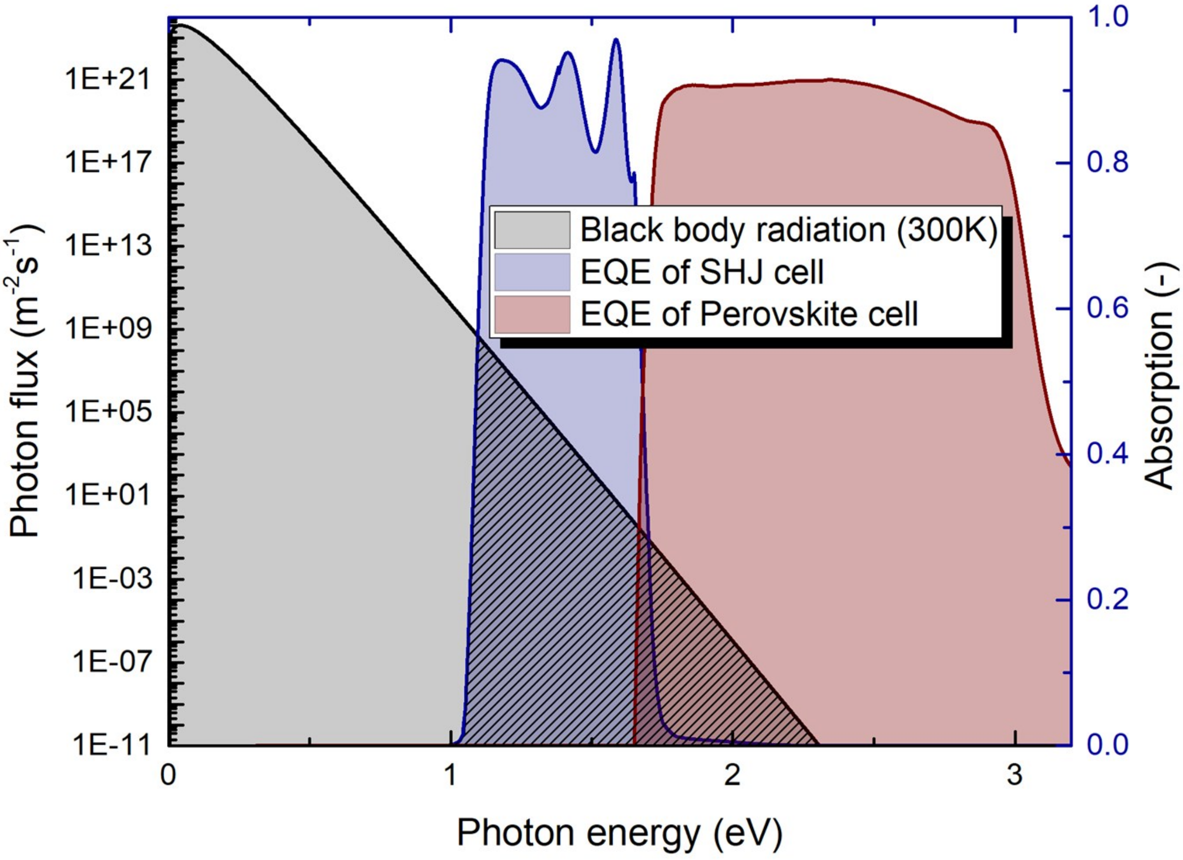

Figure S2: Black body radiation photon flux at T = 300 K overlapping with EQE of SHJ absorber and perovskite absorber integrated into a tandem device.

Since J_0 is influenced by the bandgap of the absorbing material and the temperature of the solar cell, we show the calculated J_0 for shifted bandgaps of the modelled EQE and specific equivalent circuit parameters of perovskite device at different temperatures in Figure S3 and compare it to detailed balance values, which have been calculated without parasitic resistances, m = 1 and EQE = 1 for $E > E_g$. As expected, we find that lower temperatures and higher bandgaps lead to a monotonic decrease of the reverse saturation current.

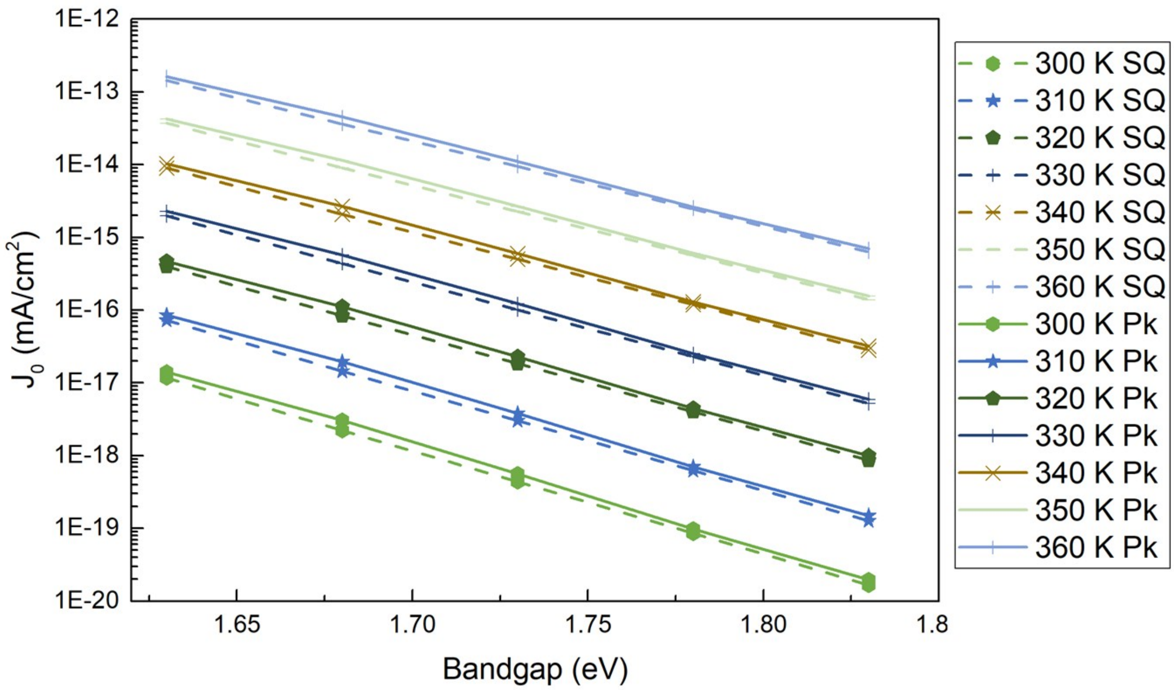

Figure S3: J_0 dependence on bandgap and temperature. Once calculated by detailed balance limit, where no parasistic resistance, m = 1 and EQE = 1 for $E > E_g$ (dashed line and labelled as SQ); once calculated by using calculated EQE of perovskite device and using specific equivalent circuit parameters (continuous line and labelled as Pk).

All of the specific equivalent circuit parameters (m, R_S, $R_{SH,}$ EQE_{EL}) were extracted from reported J(V) curves in literature by fitting the currently highest performing solar cell to the equation above. The used values for a perovskite cell[12] were $m = 1.0$, $R_S = 4.2*10^{-4}\ \Omega$, $R_{SH} = 0.5\ \Omega$ and $EQE_{EL} = 1$ %; for the SHJ cell[13] $m = 1.04$, $R_S = 4.0*10^{-5}\ \Omega$, $R_{SH} = 10\ k\Omega$ and $EQE_{EL} = 0.56$ %. Since the single-diode equation with parasitic resistances is an implicit function, the method presented by Jain et al.[14] was used to derive an analytical solution for an explicit equation that can be calculated numerically by using the W-function.

Depending on the interconnection of the tandem stack, the maximum power output was calculated in two different ways. In a 2-terminal tandem device the J(V) curves of both absorbing layers are combined by taking the lower current producing cell and calculating the corresponding limited current J(V) characteristic of the other cell[15]. Subsequently the power at maximum power point of the combined JV curve was determined. In a 4-terminal device the maximum power point of each cell J(V) was determined separately and then the powers were added up. The PCE was then determined by dividing the tandem stack power output with the integrated power from the solar spectrum. It should be noted that no optical penalty has been introduced for 4T devices (they were treated as if they were connected seamlessly together). Furthermore, no additional series resistance losses or power electronics losses were accounted for.

The annual energy yield calculations were carried out by using typical meteorological year (TMY) spectral data from NREL. They can be found in a well-organized database (NSRDB) for many locations in the USA[16]. The TMY data includes the global horizontal irradiance spectrum as well as the direct normal irradiance spectrum in the wavelength region from 300 – 1800 nm for every hour of a typical meteorological year. Since the measured spectra are only available up to 1800 nm and ca. 4 % of the spectral power lies in the IR region from 1800 nm – 4000 nm, this would lead to a slightly unprecise performance determination. Therefore, a scaled tail of the AM1.5 spectrum was attached to the measured spectra. Typical results of this tail attachment can be seen in Figure S7. In a pre-processing step, for every hour of the year, the incident angle of the direct irradiance beam towards the panel is determined. It depends on the location and on the tracking mechanism, which can be a fixed panel (at an optimal fixed tilt angle[17]), a one-axis (with tilted rotation axis), or a two-axis sun tracking system. The fixed tilt angles of 33.33 °, 39.19 ° and 29.16 ° were chosen for the locations Golden (CO), Seattle (WA) and Mohave desert (CA). Furthermore, the diffuse light distribution is modelled with the motivation to create a real world scenario, therefore instead of assuming isotropic distribution, the entire hemispherical distribution (broken into a grid of 900 nodes for numerical approximation) of the diffuse light radiance is calculated with the Brunger-Hooper model[18] and the data is grouped for accurate incidence angles of the distributed sky elements towards the fixed or tracked panel (see Figure S4). The pre-processed irradiances and their corresponding incidence angles were then fed into the previously described transfer matrix model and a maximum power output was calculated by summing up all hemispherical contributions. Repeating this process for every hour of the year and summing up the hourly power outputs multiplied with 3600 seconds/hour (for hourly energy yield), returns the annual energy yield for a particular tandem solar cell stack (2T or 4T) at a particular location in the USA with one of the three tracking solutions.

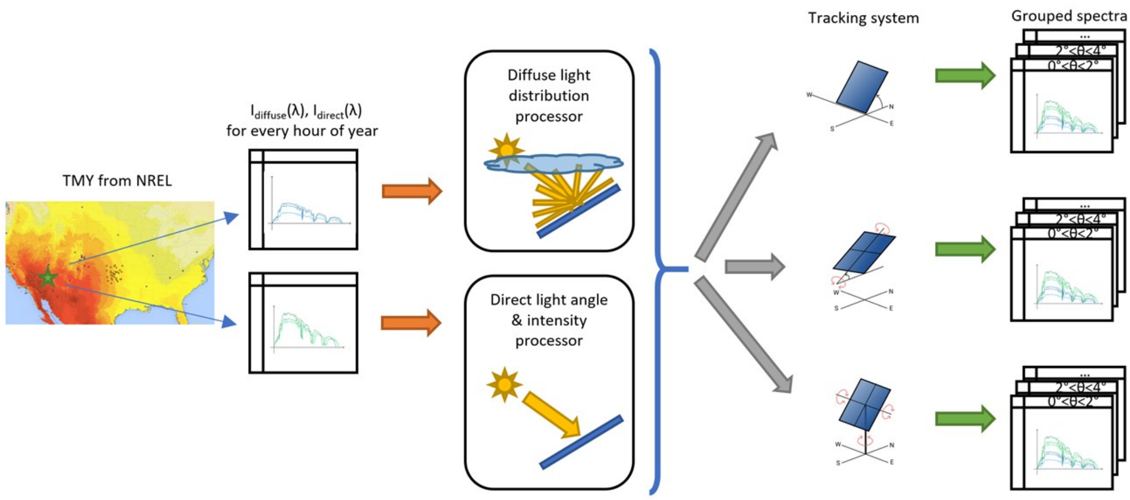

Figure S4: Illustration of the pre-processing method used for the modelling of real world solar spectra needed for the input of energy yield simulations of solar cells.

In order to not only calculate the annual energy yield but to optimise the entire material stack for maximum energy yield, the code had to be optimized and the algorithm parallelized for cluster computation. For the global optimisation, a differential evolution algorithm[19] was used, which is inherently faster than a brute force optimisation. However, some optimisations were also calculated with the latter for local and global maxima analysis.

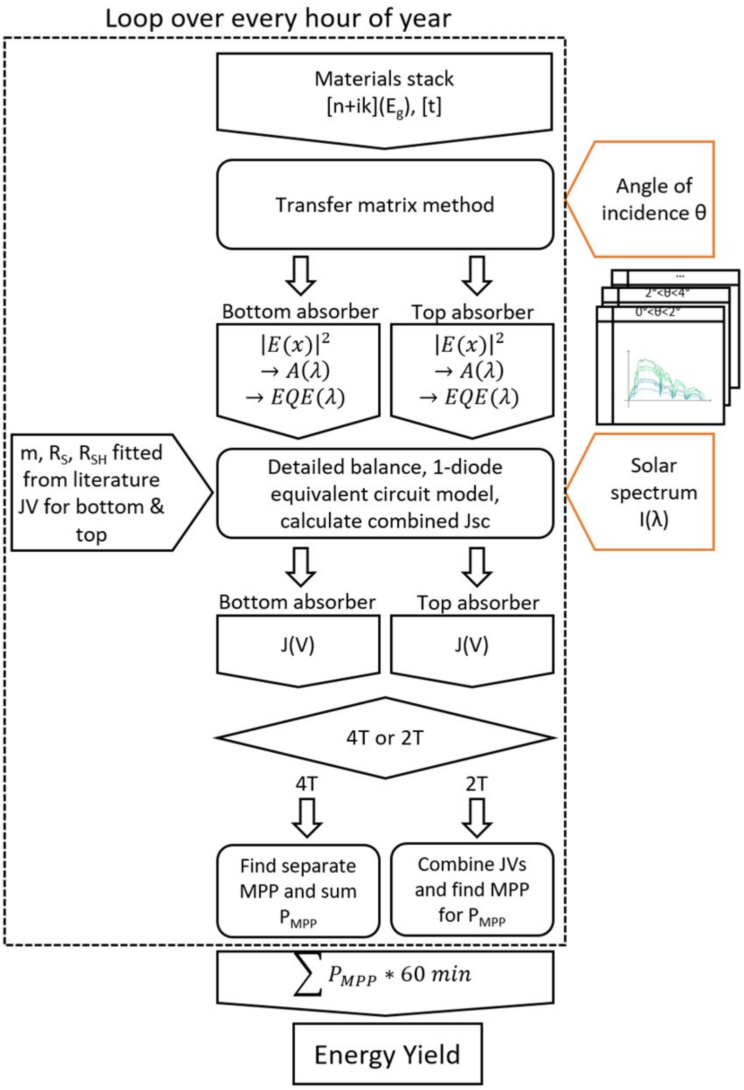

Figure S5: Simulation process for annual energy yield calculation of tandem solar cell stack.

Supporting Figures and Tables

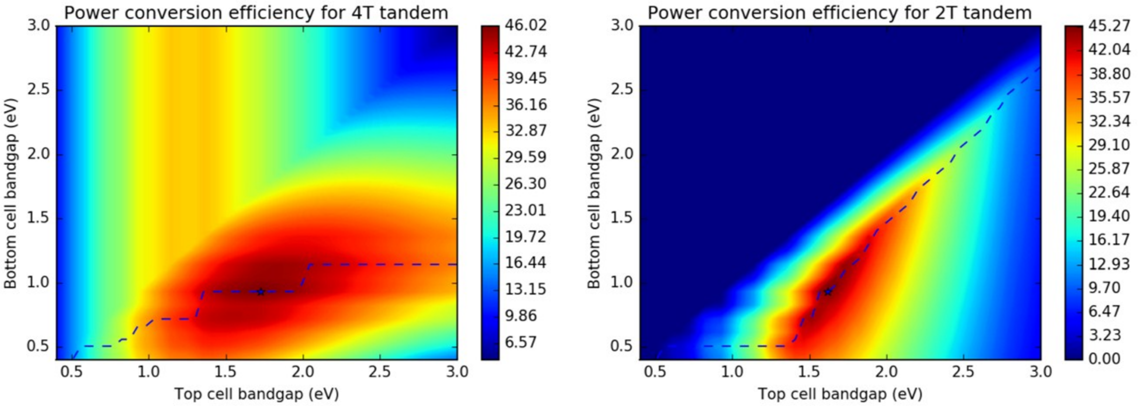

Figure S6: Combined tandem power conversion efficiency for different top cell and bottom cell bandgap combinations in 4T and 2T configurations following the Shockley Queisser limit.

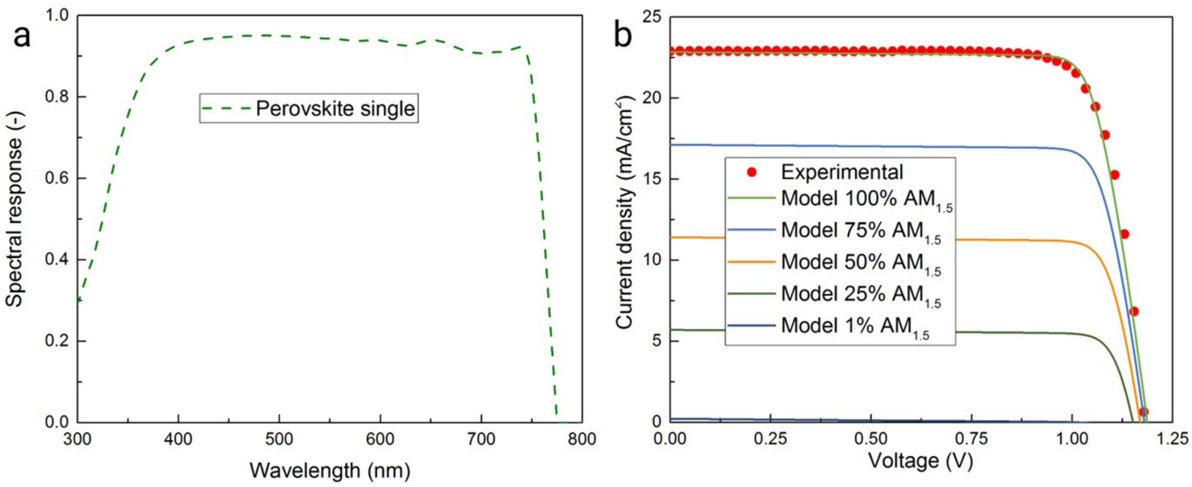

Figure S7: Simulated EQE spectrum of single-junction perovskite device (a). Experimentally measured[12] and modelled JV curves for different AM 1.5 spectrum scaling (b). The ideal diode equation parameters and radiative efficiency that lead to these fits are m = 1.0, $R_S = 4.2*10^{-4}\ \Omega$, $R_{SH} = 0.5\ \Omega$ and EQE_{EL} = 1%. Notably, the fitting does not match the experimental shape perfectly, which is likely to come from the diffusivity of ions that still causes a slight hysteresis effect[27].

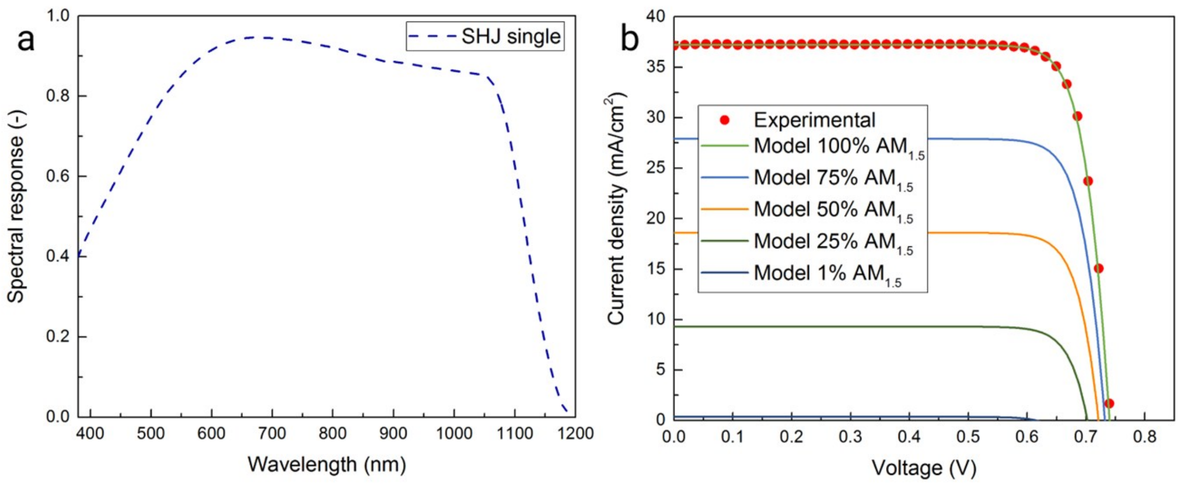

Figure S8: Simulated EQE spectrum of single-junction SHJ device (a). Experimentally measured[13] and modelled JV curves for different AM 1.5 spectrum scaling (b). The ideal diode equation parameters and radiative efficiency that lead to these fits are m = 1.04, $R_S = 4.0*10^{-5}\ \Omega$, $R_{SH} = 10\ k\Omega$ and EQE_{EL} = 0.56%

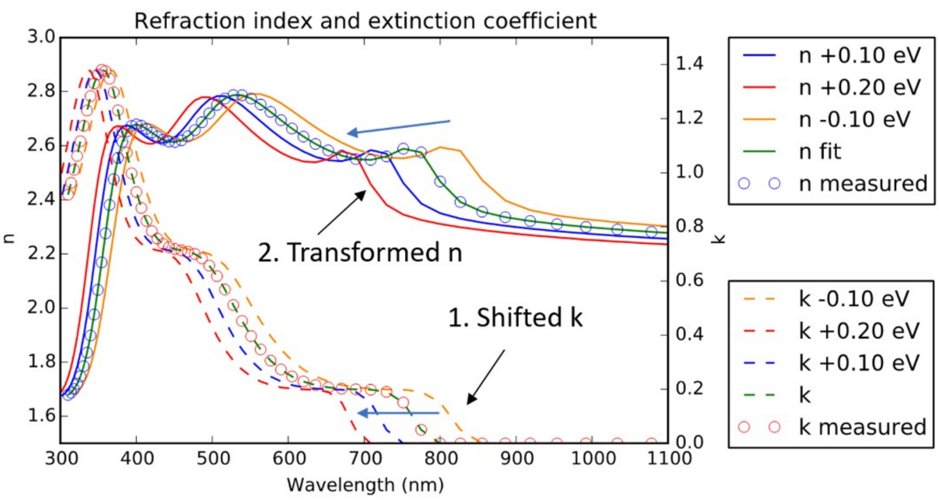

Figure S9: Shifted extinction coefficients and corresponding Kramers-Kronig transformed refractive index spectra.

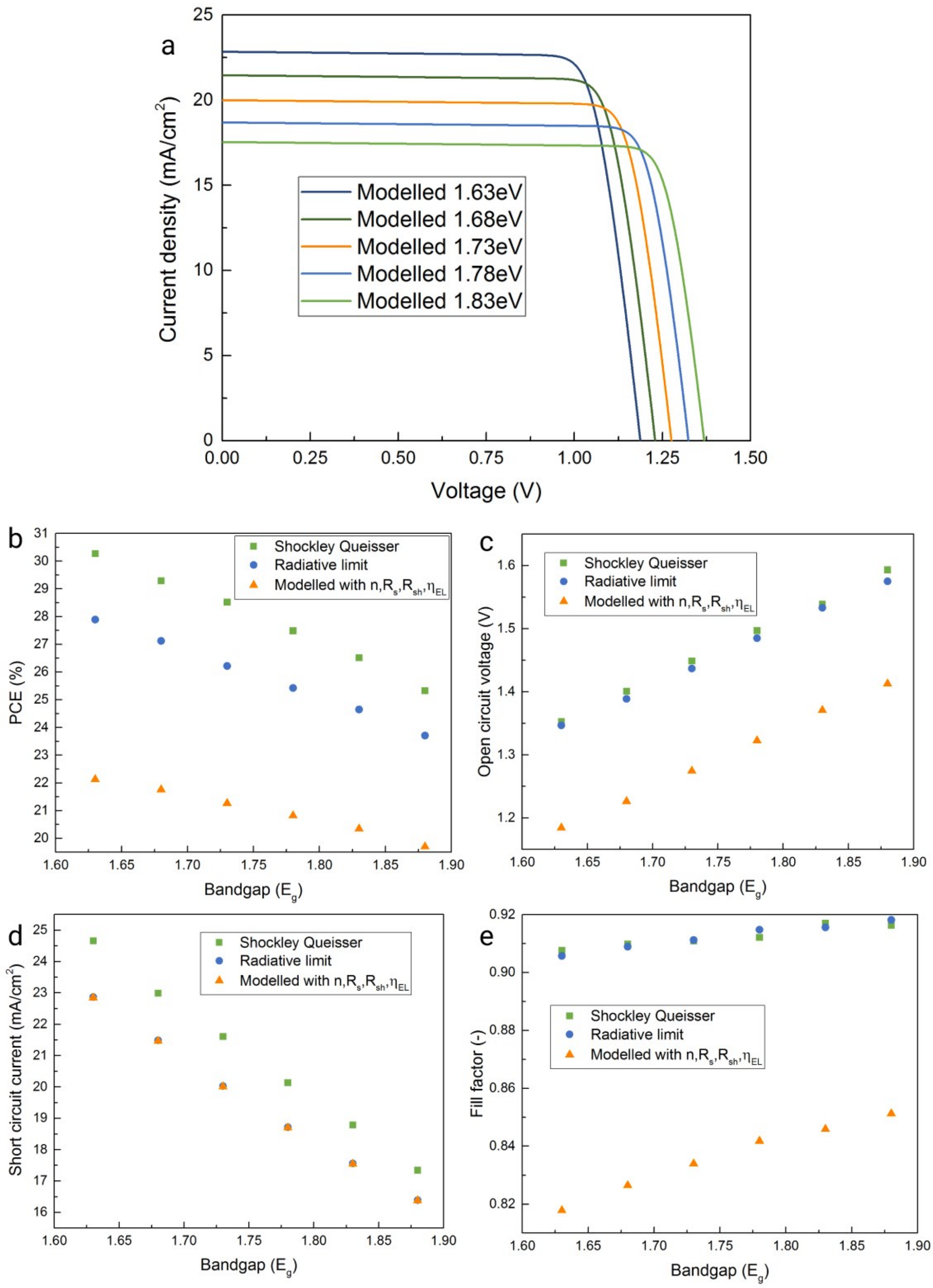

Figure S10: Modelled JV curves for shifted bandgaps of perovskite device (a). Comparison of PCE (b) V_{OC} (c), J_{SC} (d) and FF (e) for fitted one-diode model, radiative-limit model (m=1, simulated device EQE and no parasitic resistances) and detailed balance model (m =1 , EQE = 1 for E > E_g and no parasitic resistances).

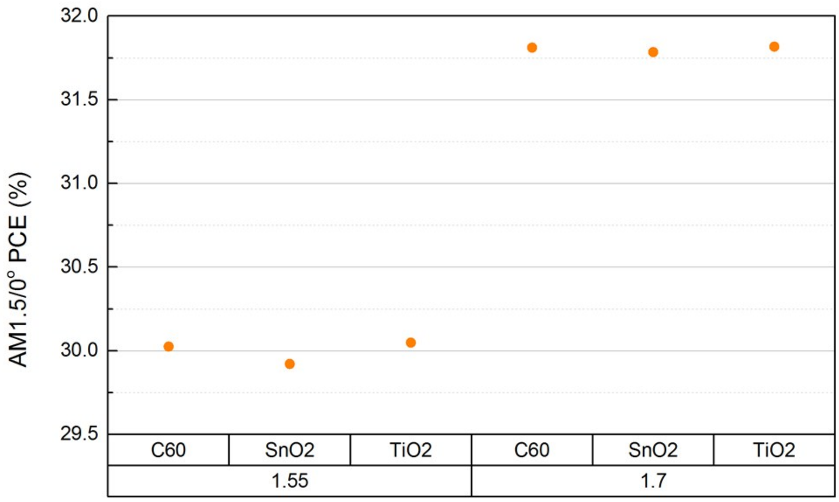

Figure S11: PCE for optimised 2T tandem devices with different electron transporting layers (C_{60}, SnO_2, TiO_2) for perovskite bandgaps of 1.55 eV and 1.70 eV.

Table S1: Tabulated geographic and meteorological data for locations Golden, Seattle and Mohave desert. Data was derived from NREL NSRDB[16] for the year 2015.

Location:	Golden, CO	Seattle, WA	Mohave Desert, CA
Latitude:	39.79°	47.49 °	34.29°
Altitude:	1820 m	139 m	646 m
Annual global horizontal irradiance:	1576 kWh/m^2	1295 kWh/m^2	2140 kWh/m^2
Annual direct normal irradiance:	1863 kWh/m^2	1482 kWh/m^2	2841 kWh/m^2
Annual diffuse horizontal irradiance:	572 kWh/m^2	503 kWh/m^2	452 kWh/m^2
Clear sky sun hours:	1701 h	1684 h	3255 h
Average annual precipitation(cm):	62.2 cm	94.3 cm	11.4 cm
Average temperature:	8.6 °C	13.0 °C	20.5 °C

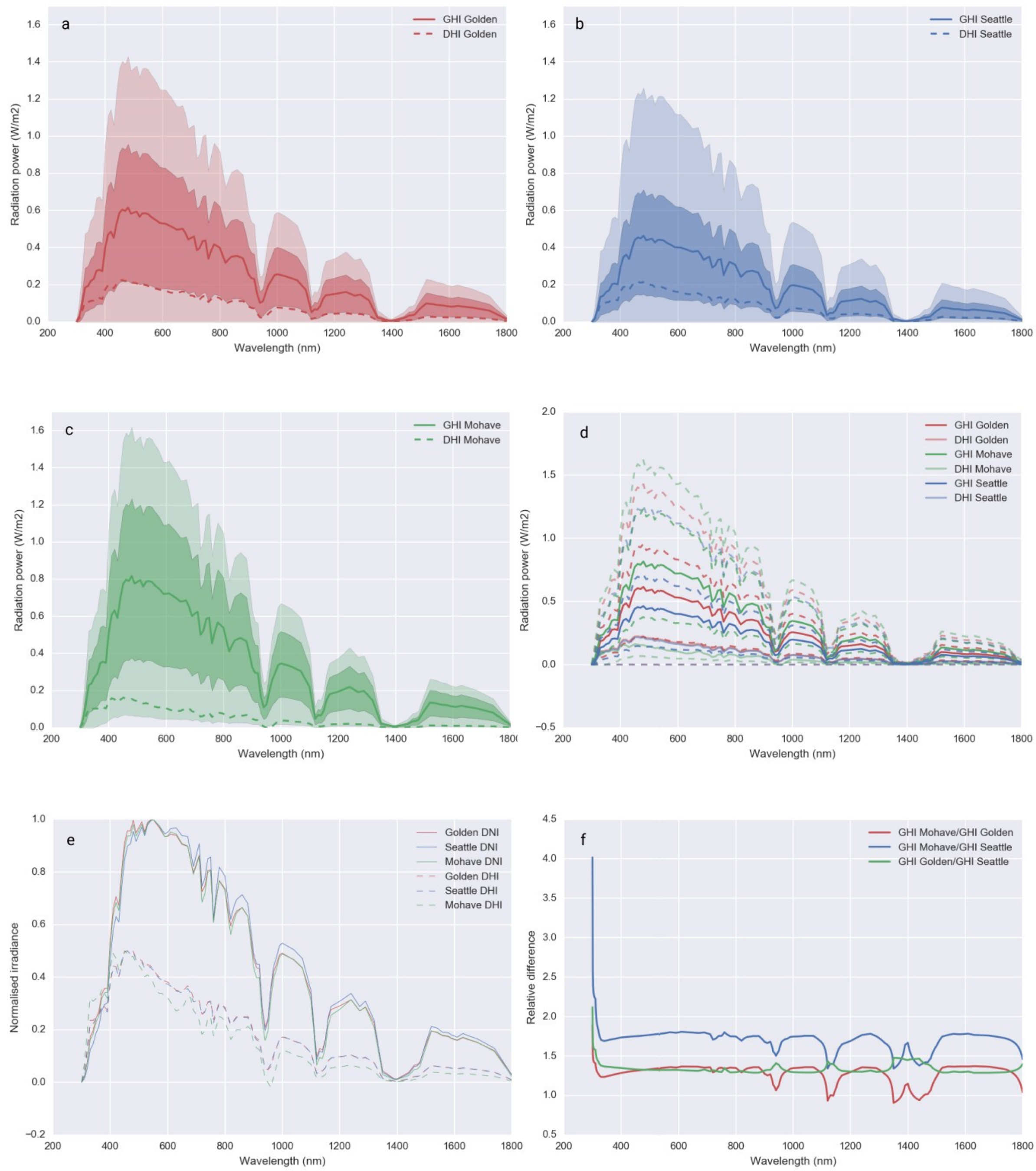

Figure S12: Diffuse horizontal irradiance and global horizontal irradiance spectrum with 25^{th} - 75^{th} and 5^{th} – 95^{th} percentile representation in Golden (a), Seattle (b) and Mohave desert (c). Comparison of DHI and GHI spectra of all three locations at correct scale (d) and DHI and DNI spectra of all three locations at normalised scales (e). Plot of the fractions of GHI spectra pairs to demonstrate non-constant scaling (f).

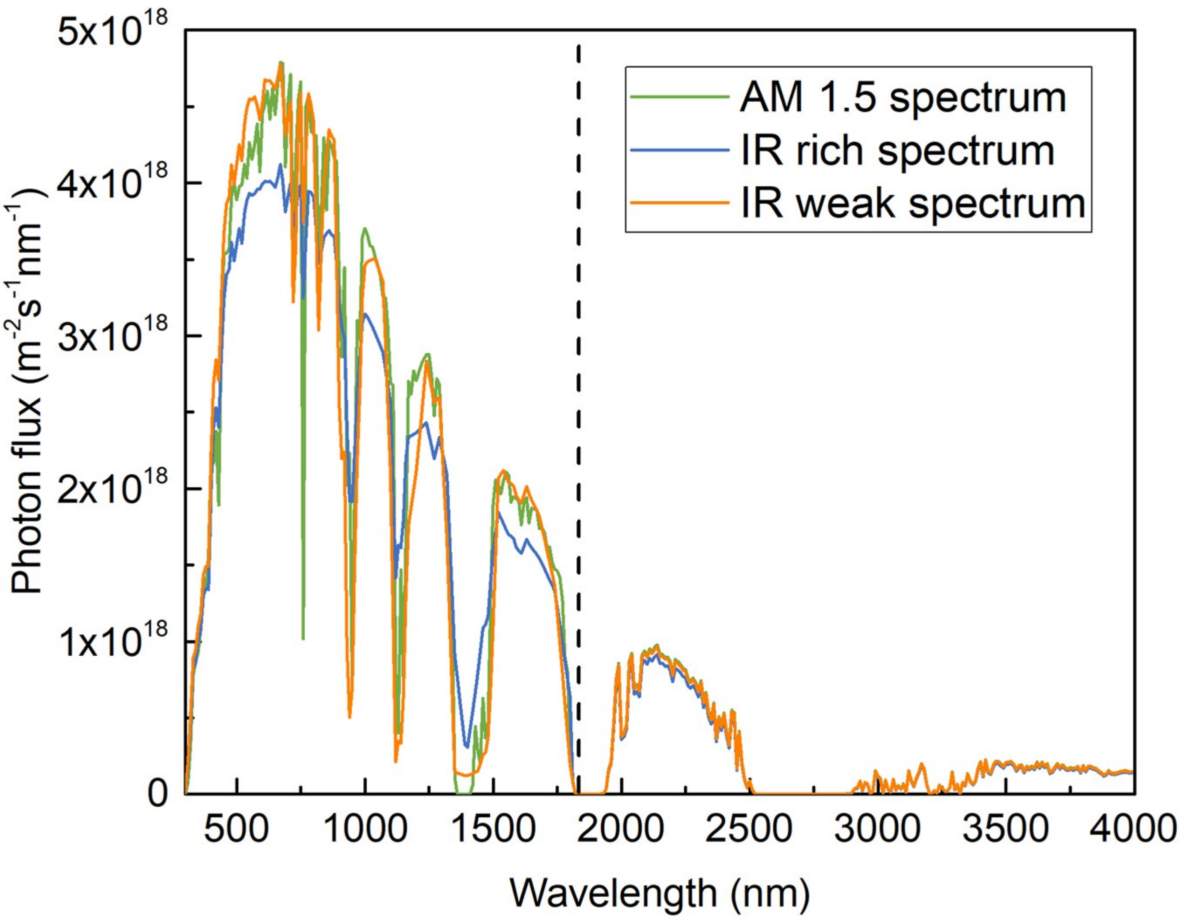

Figure S13: Comparison of photon flux of IR rich and IR weak solar spectra in comparison to AM1.5 spectrum.

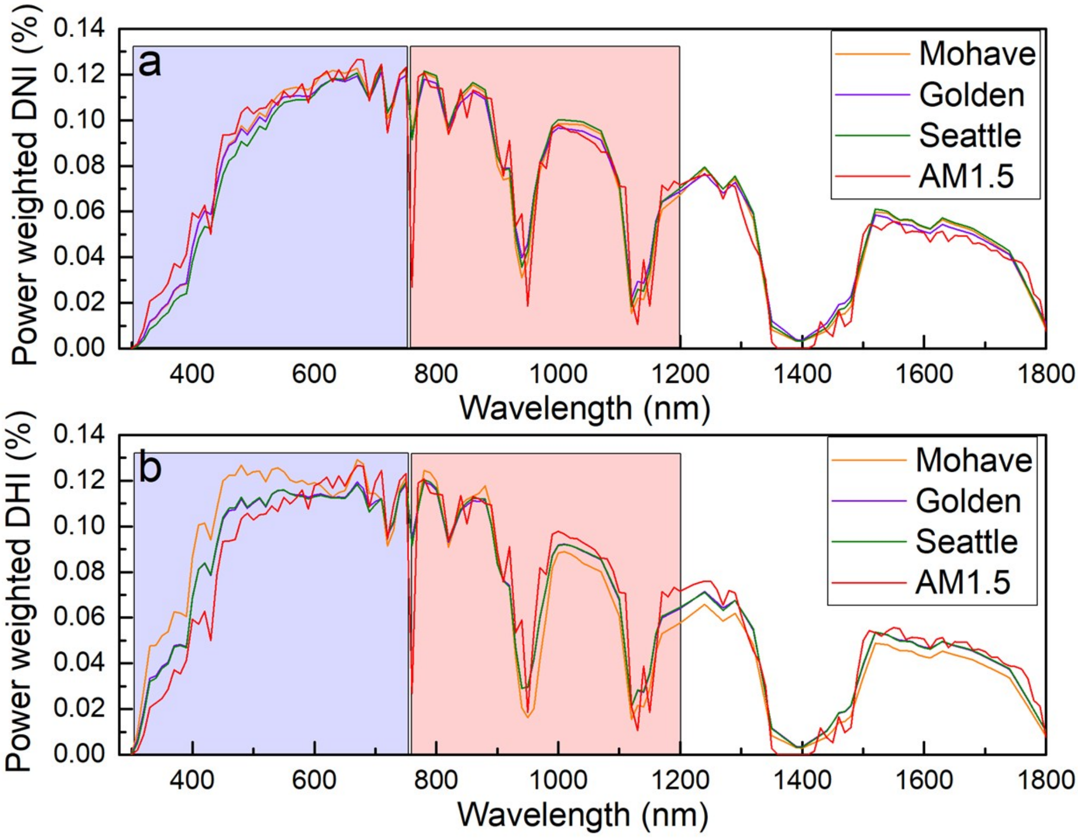

Figure S14: Integrated photon flux weighted average (a) direct normal irradiance and (b) diffuse horizontal irradiance of different locations and compared to AM1.5 spectrum. Spectra have been normalized to have an integrated value of 100% within wavelength range 280 – 1800 nm. The blue and red regions indicate the absorption ranges of perovskite and Si absorber respectively.

Table S2: Tabulated data for integrated percentage of photon flux weighted average direct normal irradiance (DNI) and diffuse horizontal irradiance (DHI) spectra for the red and blue wavelength regions as indicated in Figure S14. The third and fourth column in every sector contain the relative gain compared to the AM1.5 spectrum.

	Blue (280 – 760 nm)				Red (760 – 1200 nm)			
	DNI (%)	DHI (%)	DNI/AM1.5 (%)	DHI/AM1.5 (%)	DNI (%)	DHI (%)	DNI/AM1.5 (%)	DHI/AM1.5 (%)
Mohave	36.87	44.12	-3.36	15.65	35.98	33.06	0.34	-7.82
Golden	36.22	40.06	-5.06	5.02	36.49	34.64	1.76	-3.40
Seattle	35.08	39.94	-8.05	4.70	37.03	34.75	3.26	-3.11
AM 1.5	38.15	38.15	0.00	0.00	35.86	35.86	0.00	0.00

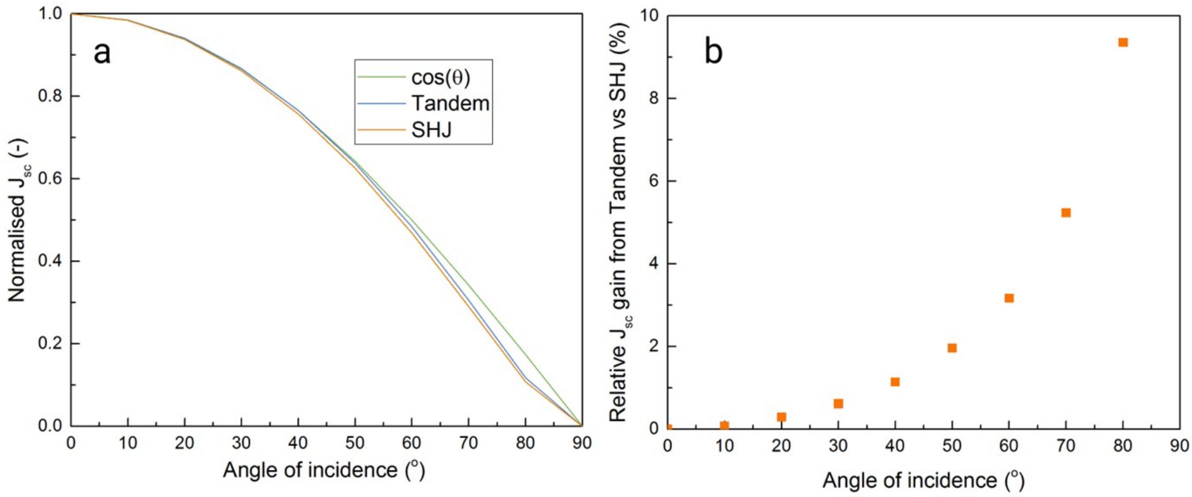

Figure S15: Angle dependence of normalised J_{SC} for SHJ device and 2T tandem device compared to cosine dependence (a). Angle dependent relative difference in normalised J_{SC} of 2T tandem to SHJ device (b).

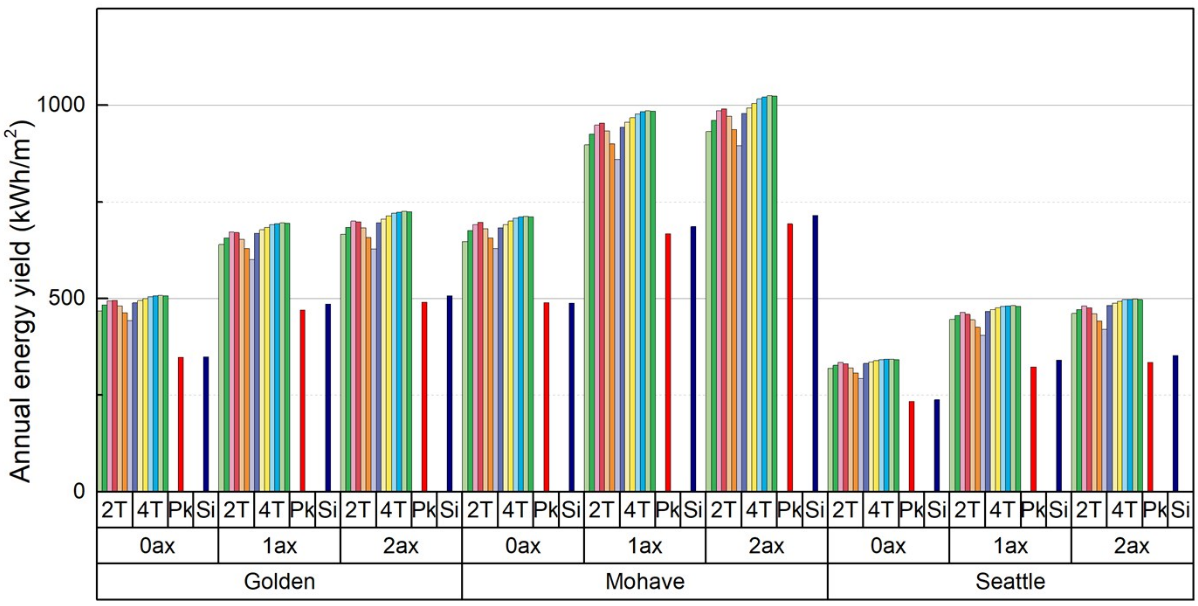

Figure S16: Annual energy yield of optimised 2T, 4T, single junction perovskite and SHJ devices at three locations for different tracking systems, ordered by ascending bandgaps.

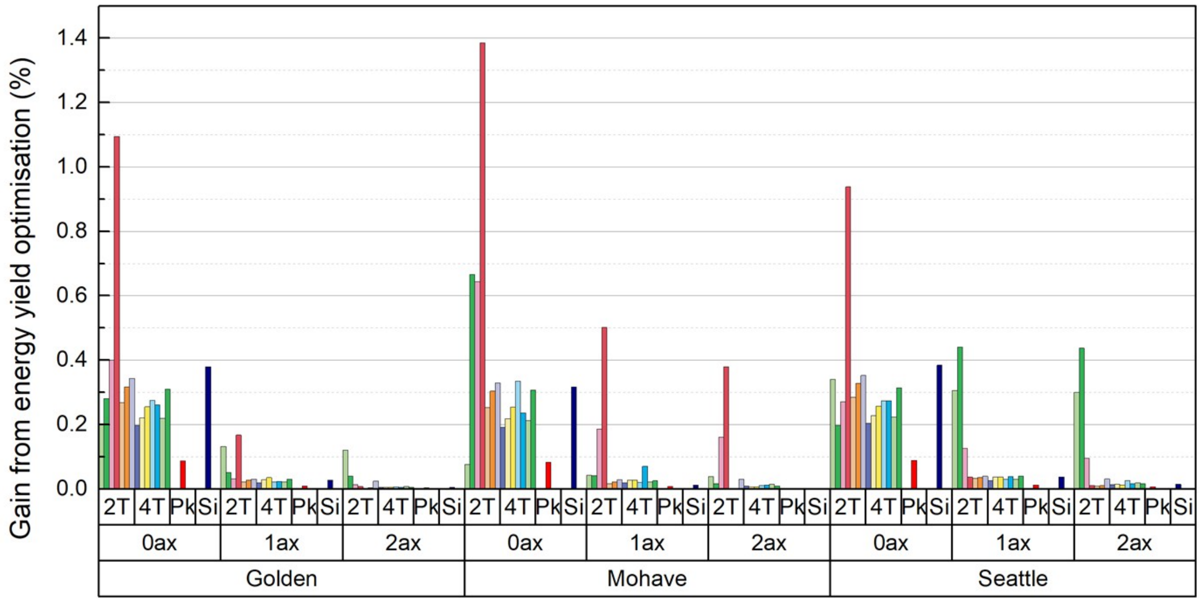

Figure S17: Relative energy yield gain of 2T, 4T, single junction perovskite and SHJ devices optimised for energy yield compared to devices optimised for $AM_{1.5}/0°$ PCE at three locations for different tracking systems, ordered by ascending bandgaps.

Table S3: Layer thicknesses of optimised 2T tandem devices with 1.65 eV perovskite band gap.

	Golden fixed	Golden 1-axis	Golden 2-axis	Mohave fixed	Mohave 1-axis	Mohave 2-axis	Seattle fixed	Seattle 1-axis	Seattle 2-axis
MgF_2 (nm)	111	102	100	114	104	103	112	104	103
ITO (nm)	60	60	60	60	60	60	60	60	60
Spiro (nm)	50	50	50	50	50	50	50	50	50
Perovskite 1.65 eV (nm)	1012	1220	1211	801	1002	1000	1250	1428	1423
C60 (nm)	10	10	10	10	10	10	10	10	10
ITO (nm)	20	20	20	20	20	20	20	20	20
SHJ (mm)	> 1	> 1	> 1	> 1	> 1	> 1	> 1	> 1	> 1
ITO (nm)	150	150	150	150	150	150	150	150	150
Ag (nm)	300	300	300	300	300	300	300	300	300

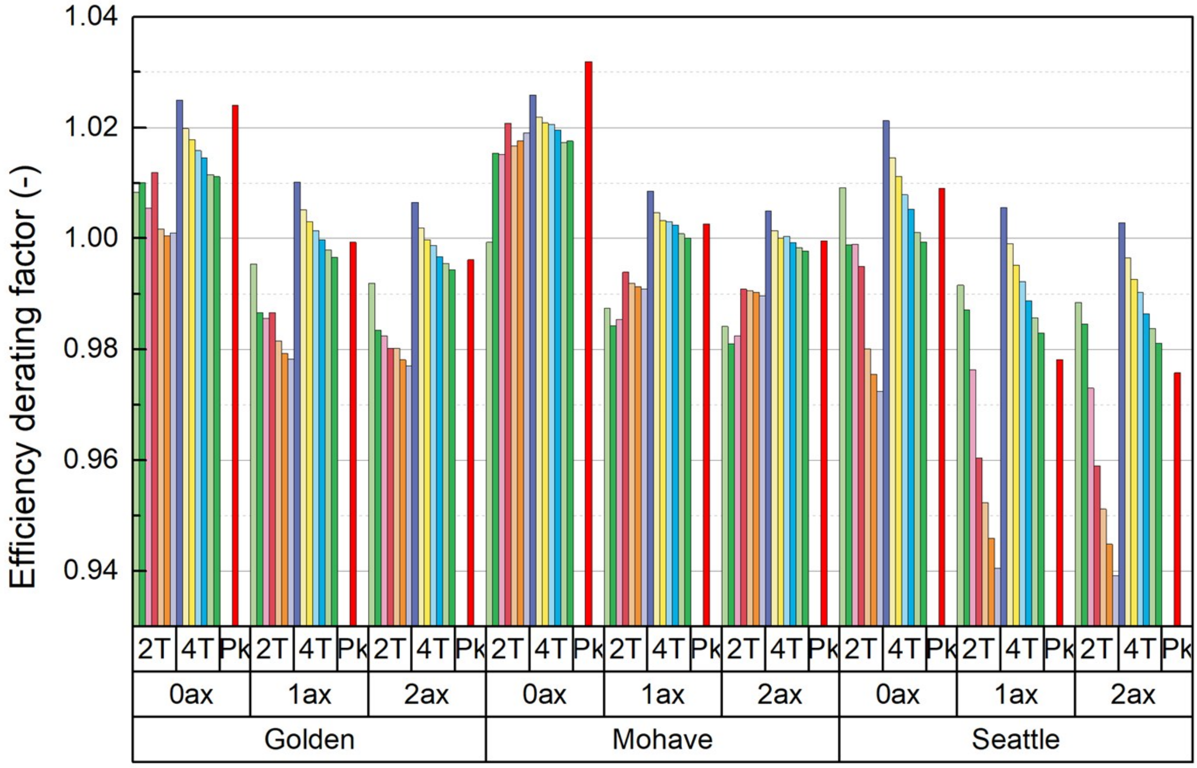

Figure S18: Efficiency derating factor of optimised 2T, 4T and single junction perovskite devices at three locations for different tracking systems, ordered by ascending bandgaps.

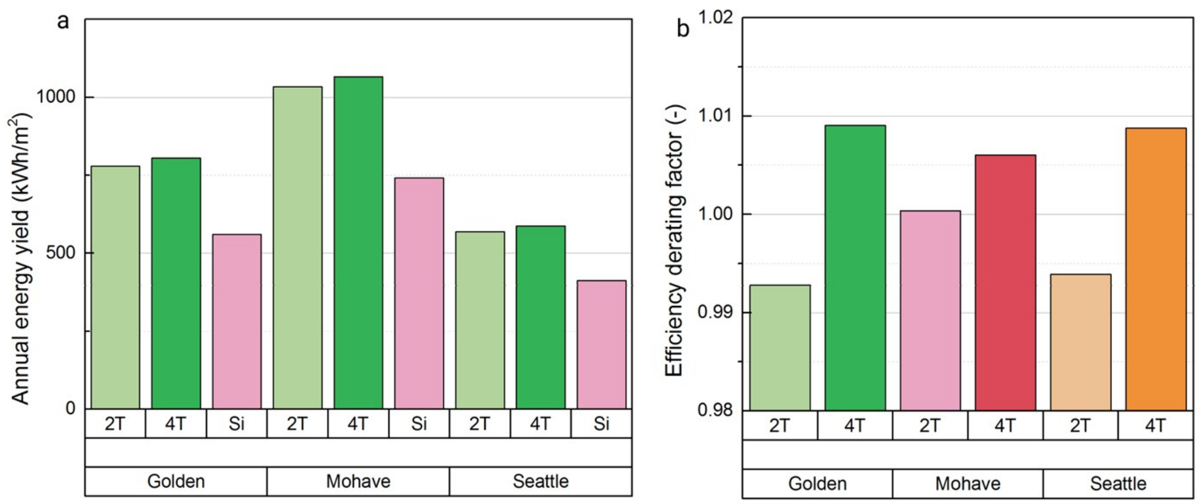

Figure S19: Annual energy yield (a) and efficiency derating factors (b) of best performing optimised devices for various tracking systems and with neglected angle of incidence at different locations.

Table S4: Tabulated simulation results of all locations, device architectures and tracking systems with the respective bandgap variations. The results are categorized in (1) PCE for the stacks that were optimised for highest AM1.5/0° efficiency, (2) PCE for stacks that were optimised for highest EY, (3) EY for stacks optimised for highest AM1.5/0° efficiency, (4) EY for stacks optimised for highest EY, (5) the gain of EY from optimising for EY vs optimising for AM1.5/0° efficiency, (6) the resulting capacity factor for the EY optimised stacks and (7) the corresponding derating factor when compared to SHJ single junction devices.

Place	Stack	Track	E_g (eV)	PCE opt $AM_{1.5}$ (%)	PCE opt EY (%)	EY opt $AM_{1.5}$ (kWh/ m^2)	EY opt EY (kWh/ m^2)	EY gain (%)	Capacity factor (kWh/ W_p)	De-rating factor (-)
Golden	Si	0ax	1.1	22.66	22.57	347.95	349.27	0.38	1.55	1.00
Golden	Pk	0ax	1.65	21.98	21.96	347.73	348.04	0.09	1.59	1.02
Golden	2T	0ax	1.55	30.03	29.96	466.72	467.66	0.20	1.56	1.01
Golden	2T	0ax	1.6	31.07	30.90	481.77	483.12	0.28	1.56	1.01
Golden	2T	0ax	1.65	31.81	31.76	492.36	494.33	0.40	1.56	1.01
Golden	2T	0ax	1.7	31.81	31.60	489.55	494.91	1.09	1.57	1.01
Golden	2T	0ax	1.75	31.08	30.99	479.12	480.40	0.27	1.55	1.00
Golden	2T	0ax	1.8	29.99	29.88	461.30	462.76	0.32	1.55	1.00
Golden	2T	0ax	1.85	28.68	28.57	441.18	442.69	0.34	1.55	1.00
Golden	4T	0ax	1.55	30.87	30.81	487.82	488.78	0.20	1.59	1.02
Golden	4T	0ax	1.6	31.44	31.35	493.69	494.77	0.22	1.58	1.02
Golden	4T	0ax	1.65	31.86	31.76	499.05	500.32	0.26	1.58	1.02
Golden	4T	0ax	1.7	32.20	32.10	503.39	504.77	0.27	1.57	1.02
Golden	4T	0ax	1.75	32.40	32.29	505.68	507.00	0.26	1.57	1.01
Golden	4T	0ax	1.8	32.53	32.44	506.75	507.86	0.22	1.57	1.01
Golden	4T	0ax	1.85	32.52	32.40	505.51	507.07	0.31	1.57	1.01
Golden	Si	1ax	1.1	22.66	22.65	485.51	485.64	0.03	2.14	1.00
Golden	Pk	1ax	1.65	21.98	21.98	470.79	470.83	0.01	2.14	1.00
Golden	2T	1ax	1.55	30.03	29.99	639.18	640.03	0.13	2.13	1.00
Golden	2T	1ax	1.6	31.07	31.05	656.33	656.66	0.05	2.12	0.99
Golden	2T	1ax	1.65	31.81	31.79	671.60	671.81	0.03	2.11	0.99
Golden	2T	1ax	1.7	31.81	31.69	669.23	670.35	0.17	2.12	0.99
Golden	2T	1ax	1.75	31.08	31.07	653.65	653.80	0.02	2.10	0.98
Golden	2T	1ax	1.8	29.99	29.98	629.23	629.41	0.03	2.10	0.98
Golden	2T	1ax	1.85	28.68	28.67	601.12	601.31	0.03	2.10	0.98
Golden	4T	1ax	1.55	30.87	30.87	668.37	668.50	0.02	2.17	1.01

Golden	4T	1ax	1.6	31.44	31.43	677.18	677.37	0.03	2.15	1.01
Golden	4T	1ax	1.65	31.86	31.85	684.64	684.88	0.04	2.15	1.00
Golden	4T	1ax	1.7	32.20	32.19	690.97	691.12	0.02	2.15	1.00
Golden	4T	1ax	1.75	32.40	32.38	693.75	693.91	0.02	2.14	1.00
Golden	4T	1ax	1.8	32.53	32.52	695.57	695.72	0.02	2.14	1.00
Golden	4T	1ax	1.85	32.52	32.51	694.35	694.55	0.03	2.14	1.00
Golden	Si	2ax	1.1	22.66	22.66	507.70	507.73	0.01	2.24	1.00
Golden	Pk	2ax	1.65	21.98	21.98	490.61	490.62	0.00	2.23	1.00
Golden	2T	2ax	1.55	30.03	30.00	665.94	666.74	0.12	2.22	0.99
Golden	2T	2ax	1.6	31.07	31.05	684.09	684.36	0.04	2.20	0.98
Golden	2T	2ax	1.65	31.81	31.80	699.99	700.09	0.01	2.20	0.98
Golden	2T	2ax	1.7	31.81	31.81	698.58	698.64	0.01	2.20	0.98
Golden	2T	2ax	1.75	31.08	31.08	682.61	682.62	0.00	2.20	0.98
Golden	2T	2ax	1.8	29.99	29.99	657.29	657.31	0.00	2.19	0.98
Golden	2T	2ax	1.85	28.68	28.68	627.62	627.77	0.02	2.19	0.98
Golden	4T	2ax	1.55	30.87	30.87	696.30	696.33	0.00	2.26	1.01
Golden	4T	2ax	1.6	31.44	31.44	705.85	705.89	0.01	2.25	1.00
Golden	4T	2ax	1.65	31.86	31.86	713.75	713.78	0.01	2.24	1.00
Golden	4T	2ax	1.7	32.20	32.20	720.54	720.59	0.01	2.24	1.00
Golden	4T	2ax	1.75	32.40	32.39	723.45	723.49	0.01	2.23	1.00
Golden	4T	2ax	1.8	32.53	32.52	725.46	725.52	0.01	2.23	1.00
Golden	4T	2ax	1.85	32.52	32.52	724.47	724.51	0.01	2.23	0.99
Mohave	Si	0ax	1.1	22.66	22.58	486.12	487.65	0.32	2.16	1.00
Mohave	Pk	0ax	1.65	21.98	21.96	488.92	489.33	0.08	2.23	1.03
Mohave	2T	0ax	1.55	30.03	30.00	646.89	647.39	0.08	2.16	1.00
Mohave	2T	0ax	1.6	31.07	30.82	671.32	675.79	0.67	2.19	1.02
Mohave	2T	0ax	1.65	31.81	31.51	686.45	690.87	0.64	2.19	1.02
Mohave	2T	0ax	1.7	31.81	31.65	688.03	697.56	1.39	2.20	1.02
Mohave	2T	0ax	1.75	31.08	30.99	678.60	680.32	0.25	2.20	1.02
Mohave	2T	0ax	1.8	29.99	29.89	654.76	656.75	0.30	2.20	1.02
Mohave	2T	0ax	1.85	28.68	28.58	626.74	628.80	0.33	2.20	1.02
Mohave	4T	0ax	1.55	30.87	30.81	681.29	682.60	0.19	2.22	1.03
Mohave	4T	0ax	1.6	31.44	31.35	690.23	691.73	0.22	2.21	1.02
Mohave	4T	0ax	1.65	31.86	31.76	698.36	700.13	0.25	2.20	1.02
Mohave	4T	0ax	1.7	32.20	32.11	705.33	707.69	0.33	2.20	1.02
Mohave	4T	0ax	1.75	32.40	32.29	709.31	710.99	0.24	2.20	1.02
Mohave	4T	0ax	1.8	32.53	32.44	711.21	712.72	0.21	2.20	1.02
Mohave	4T	0ax	1.85	32.52	32.40	709.85	712.03	0.31	2.20	1.02
Mohave	Si	1ax	1.1	22.66	22.66	685.97	686.05	0.01	3.03	1.00
Mohave	Pk	1ax	1.65	21.98	21.98	667.16	667.21	0.01	3.04	1.00
Mohave	2T	1ax	1.55	30.03	30.01	896.97	897.36	0.04	2.99	0.99
Mohave	2T	1ax	1.6	31.07	31.05	924.91	925.30	0.04	2.98	0.98

Mohave	2T	1ax	1.65	31.81	31.79	946.90	948.66	0.19	2.98	0.99
Mohave	2T	1ax	1.7	31.81	31.70	949.25	954.01	0.50	3.01	0.99
Mohave	2T	1ax	1.75	31.08	31.07	933.18	933.33	0.02	3.00	0.99
Mohave	2T	1ax	1.8	29.99	29.98	899.88	900.08	0.02	3.00	0.99
Mohave	2T	1ax	1.85	28.68	28.67	860.07	860.32	0.03	3.00	0.99
Mohave	4T	1ax	1.55	30.87	30.87	942.55	942.73	0.02	3.05	1.01
Mohave	4T	1ax	1.6	31.44	31.43	956.04	956.30	0.03	3.04	1.00
Mohave	4T	1ax	1.65	31.86	31.85	967.39	967.65	0.03	3.04	1.00
Mohave	4T	1ax	1.7	32.20	32.19	977.57	977.77	0.02	3.04	1.00
Mohave	4T	1ax	1.75	32.40	32.39	982.36	983.05	0.07	3.04	1.00
Mohave	4T	1ax	1.8	32.53	32.52	985.32	985.53	0.02	3.03	1.00
Mohave	4T	1ax	1.85	32.52	32.51	984.17	984.43	0.03	3.03	1.00
Mohave	Si	2ax	1.1	22.66	22.66	714.96	714.97	0.00	3.16	1.00
Mohave	Pk	2ax	1.65	21.98	21.98	693.15	693.17	0.00	3.15	1.00
Mohave	2T	2ax	1.55	30.03	30.02	931.68	932.04	0.04	3.11	0.98
Mohave	2T	2ax	1.6	31.07	31.06	961.25	961.41	0.02	3.10	0.98
Mohave	2T	2ax	1.65	31.81	31.79	983.98	985.56	0.16	3.10	0.98
Mohave	2T	2ax	1.7	31.81	31.70	987.44	991.18	0.38	3.13	0.99
Mohave	2T	2ax	1.75	31.08	31.08	971.44	971.45	0.00	3.13	0.99
Mohave	2T	2ax	1.8	29.99	29.99	937.09	937.11	0.00	3.12	0.99
Mohave	2T	2ax	1.85	28.68	28.68	895.24	895.51	0.03	3.12	0.99
Mohave	4T	2ax	1.55	30.87	30.87	978.85	978.94	0.01	3.17	1.00
Mohave	4T	2ax	1.6	31.44	31.44	993.41	993.48	0.01	3.16	1.00
Mohave	4T	2ax	1.65	31.86	31.86	1005.34	1005.40	0.01	3.16	1.00
Mohave	4T	2ax	1.7	32.20	32.20	1016.20	1016.31	0.01	3.16	1.00
Mohave	4T	2ax	1.75	32.40	32.39	1021.22	1021.35	0.01	3.15	1.00
Mohave	4T	2ax	1.8	32.53	32.52	1024.41	1024.55	0.01	3.15	1.00
Mohave	4T	2ax	1.85	32.52	32.51	1023.58	1023.68	0.01	3.15	1.00
Seattle	Si	0ax	1.1	22.66	22.57	237.37	238.28	0.38	1.06	1.00
Seattle	Pk	0ax	1.65	21.98	21.96	233.73	233.94	0.09	1.07	1.01
Seattle	2T	0ax	1.55	30.03	29.93	317.83	318.91	0.34	1.07	1.01
Seattle	2T	0ax	1.6	31.07	31.01	326.34	326.98	0.20	1.05	1.00
Seattle	2T	0ax	1.65	31.81	31.69	333.34	334.25	0.27	1.05	1.00
Seattle	2T	0ax	1.7	31.81	31.59	328.75	331.84	0.94	1.05	1.00
Seattle	2T	0ax	1.75	31.08	30.98	319.71	320.62	0.28	1.03	0.98
Seattle	2T	0ax	1.8	29.99	29.88	306.78	307.79	0.33	1.03	0.98
Seattle	2T	0ax	1.85	28.68	28.57	292.32	293.35	0.35	1.03	0.97
Seattle	4T	0ax	1.55	30.87	30.80	331.48	332.16	0.20	1.08	1.02
Seattle	4T	0ax	1.6	31.44	31.34	335.00	335.76	0.23	1.07	1.01
Seattle	4T	0ax	1.65	31.81	31.76	338.21	339.08	0.26	1.07	1.01
Seattle	4T	0ax	1.7	32.20	32.10	340.70	341.63	0.27	1.06	1.01
Seattle	4T	0ax	1.75	32.40	32.29	341.77	342.71	0.27	1.06	1.01

Seattle	4T	0ax	1.8	32.53	32.44	342.11	342.87	0.22	1.06	1.00
Seattle	4T	0ax	1.85	32.52	32.40	340.79	341.86	0.31	1.06	1.00
Seattle	Si	1ax	1.1	22.66	22.65	340.20	340.33	0.04	1.50	1.00
Seattle	Pk	1ax	1.65	21.98	21.98	322.93	322.97	0.01	1.47	0.98
Seattle	2T	1ax	1.55	30.03	29.95	444.88	446.24	0.31	1.49	0.99
Seattle	2T	1ax	1.6	31.07	30.75	454.00	456.00	0.44	1.48	0.99
Seattle	2T	1ax	1.65	31.81	31.69	464.23	464.82	0.13	1.47	0.98
Seattle	2T	1ax	1.7	31.81	31.80	458.67	458.84	0.04	1.44	0.96
Seattle	2T	1ax	1.75	31.08	31.07	444.41	444.55	0.03	1.43	0.95
Seattle	2T	1ax	1.8	29.99	29.98	425.93	426.09	0.04	1.42	0.95
Seattle	2T	1ax	1.85	28.68	28.67	404.94	405.10	0.04	1.41	0.94
Seattle	4T	1ax	1.55	30.87	30.87	466.24	466.37	0.03	1.51	1.01
Seattle	4T	1ax	1.6	31.44	31.43	471.60	471.78	0.04	1.50	1.00
Seattle	4T	1ax	1.65	31.86	31.85	476.04	476.22	0.04	1.50	1.00
Seattle	4T	1ax	1.7	32.20	32.19	479.73	479.87	0.03	1.49	0.99
Seattle	4T	1ax	1.75	32.40	32.38	480.80	480.98	0.04	1.49	0.99
Seattle	4T	1ax	1.8	32.53	32.52	481.41	481.56	0.03	1.48	0.99
Seattle	4T	1ax	1.85	32.52	32.50	479.81	480.01	0.04	1.48	0.98
Seattle	Si	2ax	1.1	22.66	22.66	353.15	353.20	0.01	1.56	1.00
Seattle	Pk	2ax	1.65	21.98	21.98	334.29	334.31	0.01	1.52	0.98
Seattle	2T	2ax	1.55	30.03	29.96	460.27	461.65	0.30	1.54	0.99
Seattle	2T	2ax	1.6	31.07	30.75	469.95	472.01	0.44	1.53	0.98
Seattle	2T	2ax	1.65	31.81	31.71	480.53	480.99	0.09	1.52	0.97
Seattle	2T	2ax	1.7	31.81	31.81	475.49	475.55	0.01	1.50	0.96
Seattle	2T	2ax	1.75	31.08	31.08	460.76	460.80	0.01	1.48	0.95
Seattle	2T	2ax	1.8	29.99	29.99	441.68	441.72	0.01	1.47	0.94
Seattle	2T	2ax	1.85	28.68	28.67	419.70	419.83	0.03	1.46	0.94
Seattle	4T	2ax	1.55	30.87	30.87	482.55	482.61	0.01	1.56	1.00
Seattle	4T	2ax	1.6	31.44	31.44	488.32	488.40	0.01	1.55	1.00
Seattle	4T	2ax	1.65	31.86	31.86	492.95	493.01	0.01	1.55	0.99
Seattle	4T	2ax	1.7	32.20	32.19	496.90	497.03	0.03	1.54	0.99
Seattle	4T	2ax	1.75	32.40	32.39	497.99	498.07	0.02	1.54	0.99
Seattle	4T	2ax	1.8	32.53	32.52	498.66	498.75	0.02	1.53	0.98
Seattle	4T	2ax	1.85	32.52	32.51	497.18	497.26	0.02	1.53	0.98

Temperature considerations

Including temperature contributions into our energy yield model would require a rigorous thermodynamic treatment that should include the heat generation within the absorber material from thermalization of unutilized photon energy combined with a heat conduction model through the surrounding materials with the ambient, and a heat convection model to determine the accurate temperature within the photovoltaic material. Even though ambient temperature and wind speed measurement data is available, a correct convection model would require accurate information about the specific racking system used for the installation. In addition we would need to have knowledge of and specify all the thermal properties of all the materials employed in the cell and module packaging. In order to deliver a true energy yield estimation, it will be essential to include an estimation of cell temperature under every different illumination and ambient conditions, and the solar cell operational dependence upon temperature. However, the required input data is not readily available and it is beyond the scope of our present work to collect and include the influence of temperature in our model. However, in order to assess and illustrate how much of an influence device temperature has on the overall tandem device efficiency, in comparison to the single junction SHJ, we modelled the JV characteristics as a function of junction temperature for the single junction cells and 2T tandem cells. We present these results together with the respective temperature coefficients (TCs) in Figure S20. In semiconductors, the bandgap changes with temperature, which coincidently happens in opposite directions for Si and perovskite materials[20]. We accounted for these changes by shifting the bandgap according to the temperature difference by 0.3 meV/K for the perovskite top absorber[21] and by - 0.27 meV/K for the SHJ bottom absorber[22] before calculating the J(V) curve by using equation (1) (which includes the influence of J_0 and EQE_{EL}). We derive temperature coefficients for single junction devices of - 0.277 $\%K^{-1}$ for the SHJ and – 0.165 $\%K^{-1}$ for the perovskite device, which are slightly lower but close to the values which have been measured in the literature[23,24]. As explained by others in great detail[20,25], the V_{OC} changes account for 80-90% of the total temperature sensitivity due to significant influence of the generation-recombination balance. Therefore, the TCs could be improved by increasing the radiative efficiency, which is correlated with the recombination losses. Even though the voltage losses add up in the combined tandem device, and the short-circuit current form each sub cell becomes slightly mismatched due to the bandgap shifts (see Figure S20c), the overall temperature coefficient of 0.197 $\%K^{-1}$ which we determine is slightly decreased as compared to the single junction SHJ device. This can be explained by the fact that the FF does not decline as drastically as the FF of the single junction SHJ due to the current mismatch. These results suggests that our overall conclusions concerning differences SHJ and tandem cells in energy yield, capacity factor and derating factor, will not be influenced significantly with the complete inclusion of temperature considerations, as has already been shown in a simple temperature implementation by others[26]. Moreover, we can assume that in a real tandem device, the device temperature under operation will be lower than in a SHJ cell, since there will be less thermalisation loss, and hence less thermal gain. Nevertheless, we would expect slightly lower overall energy yields, especially when panels are deployed in hot regions. Incorporating complete consideration of thermal aspects will be the subject of a future study.

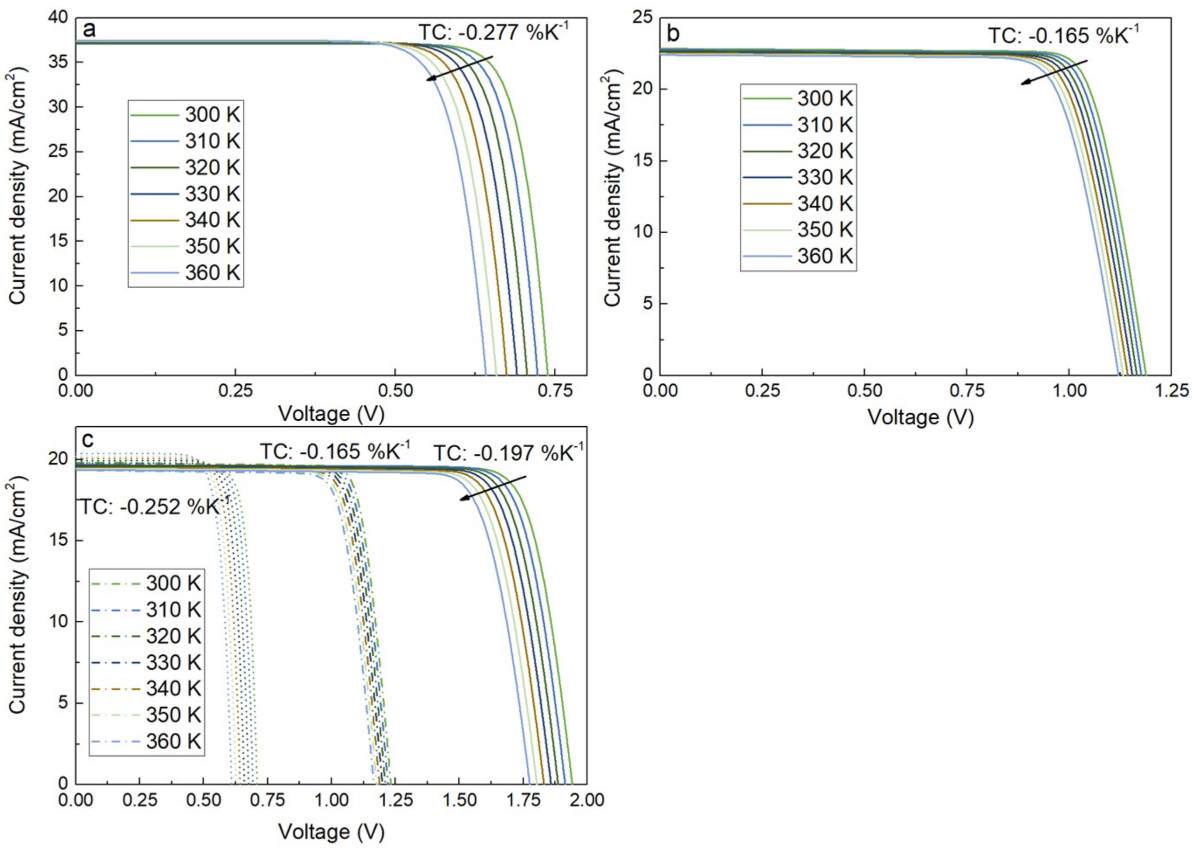

Figure S20: Modelled J(V) curves at different device temperatures and their corresponding temperature coefficients for single junction SHJ cell (a), single junction perovskite cell (b) and for 2T tandem device (c).

References:

(1) Pettersson, L. a a; Roman, L. S.; Inganäs, O. Modeling Photocurrent Action Spectra of Photovoltaic Devices Based on Organic Thin Films Modeling Photocurrent Action Spectra of Photovoltaic Devices Based on Organic Thin Films. *J. Appl. Phys.* **2011**, *487*, 487–496.

(2) Centurioni, E. Generalized Matrix Method for Calculation of Internal Light Energy Flux in Mixed Coherent and Incoherent Multilayers. *Appl. Opt.* **2005**, *44*, 7532.

(3) Ball, J. M.; Stranks, S. D.; Hörantner, M. T.; Hüttner, S.; Zhang, W.; Crossland, J. W.; Ramirez, I.; Riede, M.; Johnston, M. B.; Steiner, U.; *et al.* Optical Properties and Limiting Photocurrent of Thin-Film Perovskite Solar Cells. *Energy Environ. Sci.* **2015**, *8*, 602–609.

(4) Lin, Q.; Armin, A.; Chandra, R.; Nagiri, R.; Burn, P. L.; Meredith, P. Electro-Optics of Perovskite Solar Cells. *Nat. Photonics* **2014**, *9*, 106–112.

(5) Filipic, M.; Loper, P.; Niesen, B.; De Wolf, S.; Krc, J.; Ballif, C.; Topic, M. CH3NH3PbI3 Perovskite / Silicon Tandem Solar Cells: Characterization Based Optical Simulations. *Opt Express* **2015**, *23*, A263-78.

(6) Löper, P.; Stuckelberger, M.; Niesen, B.; Werner, J.; Filipič, M.; Moon, S.-J.; Yum, J.-H.; Topič, M.; De Wolf, S.; Ballif, C. Complex Refractive Index Spectra of CH 3 NH 3 PbI 3 Perovskite Thin Films Determined by Spectroscopic Ellipsometry and Spectrophotometry. *J. Phys. Chem. Lett.* **2015**, *6*, 66–71.

(7) McMeekin, D. P.; Sadoughi, G.; Rehman, W.; Eperon, G. E.; Saliba, M.; Horantner, M. T.; Haghighirad, A.; Sakai, N.; Korte, L.; Rech, B.; *et al.* A Mixed-Cation Lead Mixed-Halide Perovskite Absorber for Tandem Solar Cells. *Science (80-.).* **2016**, *351*, 151–155.

(8) Stern, F. Dispersion of the Index of Refraction near the Absorption Edge of Semiconductors. *Phys. Rev.* **1964**, *133*, A1653–A1664.

(9) Ohta, K.; Ishida, H. Comparison among Several Numerical Integration Methods for Kramers-Kronig Transformation. *Appl. Spectrosc.* **1988**, *42*, 952–957.

(10) Shockley, W.; Queisser, H. J. Detailed Balance Limit of Efficiency of P-N Junction Solar Cells. *J. Appl. Phys.* **1961**, *32*, 510–519.

(11) Rau, U. Reciprocity Relation between Photovoltaic Quantum Efficiency and

Electroluminescent Emission of Solar Cells. *Phys. Rev. B - Condens. Matter Mater. Phys.* **2007**, *76*, 85303.

(12) Saliba, M.; Matsui, T.; Domanski, K.; Seo, J.-Y.; Ummadisingu, A.; Zakeeruddin, S. M.; Correa-Baena, J.-P.; Tress, W. R.; Abate, A.; Hagfeldt, A.; *et al.* Incorporation of Rubidium Cations into Perovskite Solar Cells Improves Photovoltaic Performance. *Science (80-.).* **2016**.

(13) Masuko, K.; Shigematsu, M.; Hashiguchi, T.; Fujishima, D.; Kai, M.; Yoshimura, N.; Yamaguchi, T.; Ichihashi, Y.; Mishima, T.; Matsubara, N.; *et al.* Achievement of More than 25% Conversion Efficiency with Crystalline Silicon Heterojunction Solar Cell. *IEEE J. Photovoltaics* **2014**, *4*, 1433–1435.

(14) Jain, A.; Kapoor, A. Exact Analytical Solutions of the Parameters of Real Solar Cells Using Lambert W-Function. *Sol. Energy Mater. Sol. Cells* **2004**, *81*, 269–277.

(15) Hadipour, A.; de Boer, B.; Blom, P. W. M. Device Operation of Organic Tandem Solar Cells. *Org. Electron. physics, Mater. Appl.* **2008**, *9*, 617–624.

(16) NREL - National Solar Radiation Database (NSRDB) https://nsrdb.nrel.gov/ (accessed Jan 6, 2017).

(17) Landau, C. R. Optimum Tilt of Solar Panels http://www.macslab.com/optsolar.html (accessed Jan 13, 2017).

(18) Brunger, A. P.; Hooper, F. C. Anisotropic Sky Radiance Model Based on Narrow Field of View Measurements of Shortwave Radiance. *Sol. Energy* **1993**, *51*, 53–64.

(19) Storn, R.; Price, K. Differential Evolution – A Simple and Efficient Heuristic for Global Optimization over Continuous Spaces. *J. Glob. Optim.* **1997**, *11*, 341–359.

(20) Dupré, O.; Vaillon, R.; Green, M. A. Physics of the Temperature Coefficients of Solar

Cells. *Sol. Energy Mater. Sol. Cells* **2015**, *140*, 92–100.

(21) Wu, K.; Bera, A.; Ma, C.; Du, Y.; Yang, Y.; Li, L.; Wu, T.; Petrozza, A.; Angelis, F. D.; Pullerits, T.; *et al.* Temperature-Dependent Excitonic Photoluminescence of Hybrid Organometal Halide Perovskite Films. *Phys. Chem. Chem. Phys.* **2014**, *16*, 22476–22481.

(22) Green, M. A. Intrinsic Concentration, Effective Densities of States, and Effective Mass in Silicon. *J. Appl. Phys.* **1990**, *67*, 2944–2954.

(23) King, D. L.; Kratochvil, J. A.; Boyson, W. E. Temperature Coefficients for PV Modules and Arrays: Measurement Methods, Difficulties, and Results. In *Conference Record of the Twenty Sixth IEEE Photovoltaic Specialists Conference - 1997*; IEEE; pp. 1183–1186.

(24) Habisreutinger, S. N.; Leijtens, T.; Eperon, G. E.; Stranks, S. D.; Nicholas, R. J.; Snaith, H. J. Carbon Nanotube/Polymer Composites as a Highly Stable Hole Collection Layer in Perovskite Solar Cells. *Nano Lett.* **2014**, *14*, 5561–5568.

(25) Green, M. A. General Temperature Dependence of Solar Cell Performance and Implications for Device Modelling. *Prog. Photovoltaics Res. Appl.* **2003**, *11*, 333–340.

(26) Duck, B. C.; Dunbar, R. B.; Lee, O.; Anderson, K. F.; Jones, T. W.; Wilson, G. J.; Fell, C. J. Energy Yield Potential of Perovskite-Silicon Tandem Devices. In *2016 IEEE 43rd Photovoltaic Specialists Conference (PVSC)*; IEEE, 2016; pp. 1624–1629.

(27) van Reenen, S.; Kemerink, M.; Snaith, H. J. Modeling Anomalous Hysteresis in Perovskite Solar Cells. *J. Phys. Chem. Lett.* **2015**, *6*, 3808–3814.